Energy band structure of $CuInS_2$ and optical spectra of $CuInS_2$ nanocrystals

A. Shabaev
George Mason University, Fairfax, Virginia 22030, USA

M. J. Mehl and Al. L. Efros*
Naval Research Laboratory, Washington, DC 20375, USA

(Received 20 May 2015; published 27 July 2015)

Using first principles calculations we describe the energy band structure of bulk $CuInS_2$. The energy band parameters for the multiband effective mass approximation that describes the band edges of this semiconductor are obtained by fitting them to the first principles spectra. Within the multiband effective mass approximation we develop a theoretical description for the structure of band-edge levels and optical properties of the $CuInS_2$ nanocrystals. For the nanocrystals of spherical shape, the optical transitions are weakly allowed between the electron and hole ground states due to the tetragonal symmetry of the crystal lattice, resulting in a large Stokes shift of photoluminescence up to 300 meV in the smallest nanocrystals. This theory of the band-edge optical transitions in $CuInS_2$ NCs can be applied to spherical NCs made of other chalcopyrite compounds.

DOI: 10.1103/PhysRevB.92.035431 PACS number(s): 71.20.Nr, 73.21.La, 78.67.Bf

I. INTRODUCTION

Broad application of solar power calls for efficient and inexpensive solar cells. The latter requirement has intensified the search for compounds which could potentially replace crystalline Si, which is not suitable for low-cost, thin-film photovoltaic (PV) solar cells because of its very low absorption coefficient [1]. Record efficiency has been demonstrated for thin film solar cells based on wide-gap chalcopyrites, with efficiencies of 12.5% reported in $CuInS_2$ devices [2]. One of the most promising thin film technologies for solar cells is based on polycrystalline $Cu(In,Ga)Se_2$ films, which show efficiencies higher than 20% [3].

The first solar cell based on the chalcopyrite I-II-VI_2 [4] was prepared without the use of Ga, which was added into compound only 20 years later, when it was shown that alloying optimized the solar cell energy gap for the solar spectrum and significantly improved device efficiency [5]. Energy-gap engineering can be also realized by using nanocrystal (NC) quantum dots, whose energy gap could be tuned to a required value by changing the NC size. In addition, the relatively inexpensive preparation process of colloidal quantum dots and their chemical postprocessing allows one to grow low-cost thin films for solar cell PV [6–8]. A great degree of progress in this direction has been reached using lead-based compounds such as PbSe, PbS, and PbTe NCs [9–13].

Lead-based compounds, along with other traditionally used III–V and IV–VI compounds, contain toxic elements. This has led to a growing interest in use of $CuInS_2$ and $CuInSe_2$ NCs, since these have been identified as potentially less toxic materials. In addition, the absorption energy gap and photoluminescence in these materials are tunable over a wide range of the spectrum, from the near-infrared through the visible to the ultraviolet [14–17]. These flexible optical properties, combined with nontoxicity, indicate the great potential of $CuInS_2$ and $CuInSe_2$ NCs for use in a large variety of applications, including biotechnology [18–23].

In bulk $CuInS_2$, reflectivity, photoreflectivity, and photoluminescence (PL) spectra show two distinct exciton resonances associated with three excitons, A, and the degenerate excitons, BC [24]. For the A exciton, the binding energy and polariton doublet energies have been reported [25–27]. A binding energy of 18.5 meV has been measured in high-quality $CuInS_2$ single crystals [28]. Masses have been estimated using measurements of diamagnetic shift [29]. Theoretical descriptions of excitons have been developed using the limited knowledge of material parameters for chalcopyrites [30,31].

No theoretical studies can be found in the literature on the electronic and band-edge optical properties of $CuInS_2$ NCs. Experimental studies of the size dependence of absorption show only one broad absorption maximum, whose width increases with decreasing size [14–17]. The PL line measured in large $CuInS_2$ NCs is below the bulk absorption edge [15,17], and hence this line is likely associated with deep defects created by the Cu vacancies [15]. Even for bulk $CuInS_2$, the electronic band structure has been theoretically studied in a handful of publications [32,33]. Only recently have some energy band parameters for $CuInSe_2$ been extracted from the fine structure of the band-edge excitons and interband magnetoabsorption spectra [34,35].

In this paper we study the band-edge level structure and optical selection rules in spherical $CuInS_2$ NCs. The energy level structure of the NCs has been calculated using bulk energy parameters provided by our first principles calculations and extracted from available experimental data [24–30,36]. We show that the ground hole levels in these NCs have p-type symmetry and optical transitions between these levels, and the ground 1S electron state of conduction band is only weakly allowed due to a low symmetry of the crystal structure of these semiconductors. As a result the intrinsic PL of these NCs should have a significant Stokes shift from its absorption. The developed theory of the band-edge optical transitions in $CuInS_2$ NCs can be applied to spherical NCs made of other chalcopyrite compounds.

*Address correspondence to efros@nrl.navy.mil

TABLE I. Crystallographic information for $CuInS_2$ in the chalcopyrite structure at equilibrium, as determined by experiment [37] and by VASP calculations using the PBE and HSE06 functionals described in the text.

Space Group		$I\bar{4}2d$ (no. 122)		
	Cu	(4a)	(0 0 0)	
Wyckoff positions	In	(4b)	(0 0 1/2)	
	S	(8d)	(x_S 1/4 1/8)	
		Exp.	PBE	HSE06
	a (Å)	5.523	5.580	5.553
Lattice parameters	c (Å)	11.12	11.246	11.218
	x_S	0.214	0.218	0.226

II. FIRST PRINCIPLES CALCULATIONS FOR $CuInS_2$ IN THE CHALCOPYRITE ($E1_1$) STRUCTURE

Experimentally, bulk $CuInS_2$ exists in the body-centered tetragonal chalcopyrite structure (*Strukturbericht* $E1_1$) [37], described in Table I. As with many chalcopyrites [33], this structure is very close to the cubic zincblende structure, which we could obtain if, e.g., we replaced the Cu and In atoms by one species, e.g., Zn or Cd, and took $c \to 2a$ and $x_S \to 1/4$.

The electronic structure of $CuInS_2$ was determined using the Vienna *Ab-initio* Simulation Package (VASP) [38–40] with Projector Augmented Wave functions [41]. Our initial calculations used the Perdew-Burke-Ernzerhof (PBE) Generalized Gradient Approximation [42] within the Kohn-Sham *ansatz* of Density Functional Theory [43,44]. We used an energy cutoff of 280 eV and a Γ-centered $6 \times 6 \times 6$ k-point grid with 30 k points in the irreducible Brillouin zone. The initial experimental structure was allowed to relax until equilibrium was achieved. This equilibrium position did not change when we increased the density of the k-point mesh. Spin polarization and spin-orbit effects are negligible in this system, so we used the unpolarized version of the PBE functional.

As noted many years ago [32], standard DFT predicts $CuInS_2$ to be a semimetal. Jaffe and Zunger corrected for this by an *ad hoc* increase in the exchange energy [33]. We instead used the Heyd-Scuseria-Ernzerhof "HSE06" hybrid density functional [45], within VASP, setting the screening parameter `HFSCREEN` to 0.2. Starting from the PBE equilibrium structure and wave functions, we relaxed the structure using the HSE06 functional. Table I compares the PBE, HSE06, and experimental equilibrium lattice parameters. We note that the equilibrium lattice parameters a and c are better predicted by HSE06 than by PBE, but the internal sulfur position parameter x_S is better determined by PBE.

The HSE06 band structure of $CuInS_2$ is shown in Fig. 1, using the notation shown in Fig. 2. There is a direct band gap, E_g, of 1.24 eV, in reasonable agreement with the experimental value of 1.55 eV [24,33].

In cubic zincblende structures such as ZnS the valence bands at Γ are triply degenerate. The presence of indium breaks the cubic symmetry, leaving a singlet just below the doubly degenerate state at the top of the valence band, with a shift of 6.5 meV. This is shown more clearly in Fig. 3.

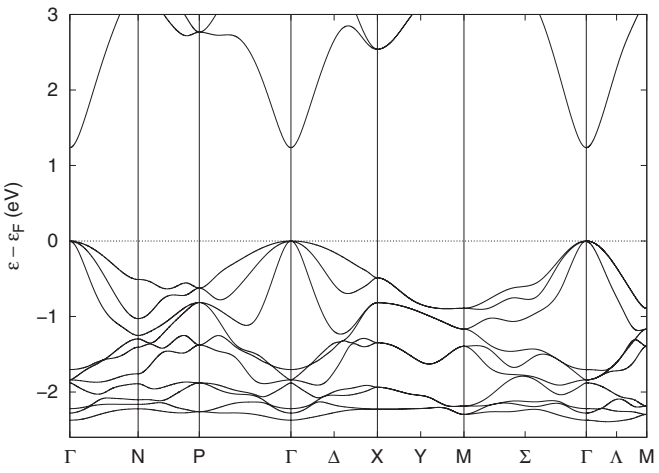

FIG. 1. The HSE06 band structure of $CuInS_2$ in the chalcopyrite structure. The direct gap is 1.23 eV, in reasonable agreement with the experimental value of 1.55 eV [24,33].

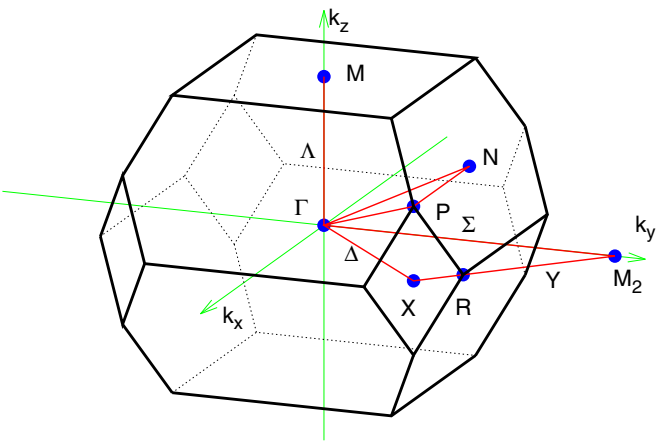

FIG. 2. (Color online) The Brillouin zone of $CuInS_2$. The special points and symmetry directions follow the conventions of Lax [46] and are used in the band structure plot of Fig. 1. Note that the orientation of the x and y axes are rotated by 45° from the usual positions.

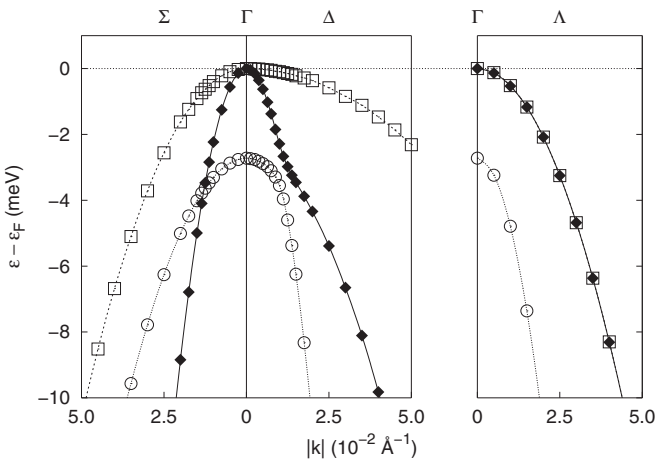

FIG. 3. A close-up view of the valence bands of $CuInS_2$ near Γ, looking along the Σ, Δ, and Λ directions (see Fig. 2). Note the splitting of the valence band into singly and doubly degenerate levels due to the tetragonal symmetry, even in the absence of spin-orbit coupling. The upper band remains doubly degenerate along Λ.

Next we turn to the energy spectra of the bulk $CuInS_2$ valence band. Preliminary information allows us to assume that the spin-orbit splitting of the valence band in $CuInS_2$ is small, and we will initially consider only the case where valence band spin-orbit splitting is $\Delta = 0$. The corresponding calculation of the energy band structure of $CuInS_2$ is shown in Fig. 1. For better understanding of the critical points of the Brillouin zone in Fig. 2 we compare the $CuInS_2$ unit cell with the unit cell of a virtual cubic crystal. The crystal structure of $CuInS_2$ has tetragonal symmetry stretched in the z direction or [001]. The [100] and [110] directions are in the plane perpendicular to the elongation.

III. MULTIBAND EFFECTIVE MASS APPROXIMATION

We will describe optical properties of NCs using the multiband $\boldsymbol{k}\cdot\boldsymbol{p}$ effective mass Hamiltonian. The conduction band can be described using the Kane model, which takes into account the coupling between the conduction and valence bands. The electron energy E_c within this model is given by Ref. [47]:

$$E_c = \frac{p^2}{2m_0}\left[\alpha + \frac{E_p}{E_g + E_c}\right], \tag{1}$$

where m_0 is the mass of a free electron, E_p is the Kane energy parameter, and α is the contribution of the remote bands to the electron effective mass. The best fit of our first principle spectrum is given by $\alpha = 0.48$ and $E_p = 7.95$ eV. For $E_c \ll E_p$, the effective mass of electron is $0.15m_0$. This value is close to experimental value of the electron effective mass $0.16m_0$ [48].

The valence band structure can be constructed by the method of invariants introduced by Luttinger [49]. The parameters of this Hamiltonian were obtained from our first principles calculations. For the valence band in spherical approximation, the method of invariants gives

$$\begin{aligned}\hat{H}_{\text{cubic}} = \frac{1}{2m_0}\big[&(\gamma_1 + 4\gamma_2)p^2 - 6\gamma_2\big(p_x^2 I_x^2 + p_y^2 I_y^2 + p_z^2 I_z^2\big)\\ &- 12\gamma_3(\{p_x,p_y\}\{I_x,I_y\} + \{p_y,p_z\}\{I_y,I_z\}\\ &+ \{p_z,p_x\}\{I_z,I_x\})\big],\end{aligned} \tag{2}$$

where γ_1, γ_2, and γ_3 are the Luttinger parameters, $\{a,b\} = (ab + ba)/2$, and $\boldsymbol{I}$ is the spin one matrix operator [49]:

$$I_x = \begin{pmatrix} 0 & 0 & 0 \\ 0 & 0 & -i \\ 0 & i & 0 \end{pmatrix}, \quad I_y = \begin{pmatrix} 0 & 0 & i \\ 0 & 0 & 0 \\ -i & 0 & 0 \end{pmatrix},$$
$$I_z = \begin{pmatrix} 0 & -i & 0 \\ i & 0 & 0 \\ 0 & 0 & 0 \end{pmatrix}. \tag{3}$$

The D_{2d} group symmetry of $CuInS_2$ allows additional invariant terms $\hat{V}_{2d}$, which can be added to the Hamiltonian in Eq. (2) [50]:

$$\hat{H}_{2d} = \hat{H}_{\text{cubic}} + \hat{V}_{2d}. \tag{4}$$

The crystal structure of $CuInS_2$ is very close the cubic zincblende structure, and we try to find the minimum number of invariants in $\hat{V}_{2d}$ which would reproduce the energy band structure shown in Fig. 3. The D_{2d} group consists of rotations around the vertical C_2 axis and two horizontal C_2 axes (U_2 axes) perpendicular to the C_2 axis plus two vertical reflection planes at a 45° angle between two horizontal C_2 axes. One can compose algebraic combinations of the projections of vector $\hat{\boldsymbol{p}}$ and pseudovector $\hat{\boldsymbol{I}}$, which are invariant with respect to the symmetry operations of the D_{2d} group [50].

For the band structure obtained from our first-principles calculation, we found that the valence band spectrum can be described by the Hamiltonian in Eq. (4) with the following addition to the cubic Hamiltonian quadratic invariants:

$$\begin{aligned}\hat{V}_{2d} = \Delta_c I_z^2 + \frac{1}{2m_0}\big[&(\gamma_{1\perp} + 4\gamma_{2\perp})\big(p_x^2 + p_y^2\big)\\ &- 6\gamma_{2\perp}\big(p_x^2 I_x^2 + p_y^2 I_y^2\big) - 12\gamma_{3\perp}\{p_x,p_y\}\{I_x,I_y\}\\ &- 6\gamma_{4\perp}\big(p_x^2 I_y^2 + p_y^2 I_x^2\big)\big].\end{aligned} \tag{5}$$

The seven Luttinger parameters γ_i $(i = 1,\ldots,7)$ which defined $\hat{H}_{2d}$ can be associated with the effective masses of the three valence subbands in various crystallographic directions. Figures 4(a)–4(c) show the spectra in the [001], [100], and [110] directions near the Γ point, where the spectrum is split by Δ_c into double and single degenerate energy states. Along the Λ line (in the [001] direction), the doubly and singly degenerate states form the heavy- and light-hole bands with the the masses $m_0/(\gamma_1 - 2\gamma_2)$ and $m_0/(\gamma_1 + 4\gamma_2)$. For the other two directions, it is convenient to introduce $\gamma_1' = \gamma_1 + \gamma_{1\perp}$, $\gamma_2' = \gamma_2 + \gamma_{2\perp}$, and $\gamma_3' = \gamma_3 + \gamma_{3\perp}$. Along the Σ line (the [100] direction in Fig. 2), one heavy-hole band with the masses $m_0/(\gamma_1' - 2\gamma_2')$ is degenerate at the Γ point with the light-hole band with the mass $m_0/(\gamma_1' + 4\gamma_2' - 6\gamma_{4\perp})$, which are both split from the other heavy-hole band with the mass of $m_0/(\gamma_1' - 2\gamma_2' - 6\gamma_{4\perp})$. Along the Δ line (the [110] direction), the spectrum is similar, but the masses are different. The light-hole mass is $m_0/(\gamma_1' + \gamma_2' + 3\gamma_3' - 3\gamma_{4\perp})$. The two heavy-hole masses are $m_0/(\gamma_1' + \gamma_2' - 3\gamma_3' - 3\gamma_{4\perp})$ and $m_0/(\gamma_1' - 2\gamma' - 6\gamma_{4\perp})$. The parameter γ_3 can be determined from the nonparabolic spectrum in direction [111]. For our first principles spectrum, the best fit is provided by $\gamma_1 = 2.63$, $\gamma_{1\perp} = -0.03$, $\gamma_2 = 0.63$, $\gamma_{2\perp} = 0.12$, $\gamma_3 = 0.8$, $\gamma_{3\perp} = 0.3$, $\gamma_{4\perp} = -0.06$, and $\Delta_c = -2.7$ meV. For the effective masses of holes, we estimate $m_A = m_B = 0.73m_0$, $m_C = 0.19m_0$ in the [001] direction, $m_A = 0.91m_0$, $m_B = 0.17m_0$, $m_C = 0.68m_0$ in the [100], and $m_A = 4.3m_0$, $m_B = 0.15m_0$, $m_C = 0.68m_0$ in the [110] direction.

The complete set of invariants for the D_{2d} group can be found in Ref. [51]. The invariant omitted in Hamiltonian (4) are two linear in momentum invariants:

$$\begin{aligned}\hat{V}_{2d}' &= u_I(I_x p_x - I_y p_y) + \bar{u}_I(I_x p_y - I_y p_x),\\ \hat{V}_{2d}'' &= u_\sigma(\sigma_x p_x - \sigma_y p_y) + \bar{u}_\sigma(\sigma_x p_y - \sigma_y p_x),\end{aligned} \tag{6}$$

and the spin-orbit interaction

$$\hat{V}_{\text{so}} = -\tfrac{1}{3}\Delta_s^{\parallel} I_z\sigma_z - \tfrac{1}{3}\Delta_s^{\perp}(I_x\sigma_x + I_y\sigma_y), \tag{7}$$

where $\sigma_{x,y,z}$ are Pauli matrices. The spin-orbit splitting modifies the masses near the Γ point where the energy dispersion is much smaller than the splitting [see Figs. 4(d)–4(f)]. For the splitting $\Delta_s = \Delta_s^{\parallel} = \Delta_s^{\perp} = -21$ meV [26,36], the effective masses are $m_A = 0.41m_0$, $m_B = 0.73m_0$, $m_C = 0.24m_0$ in the [001] direction and $m_A = 0.34m_0$, $m_B = 0.28m_0$,

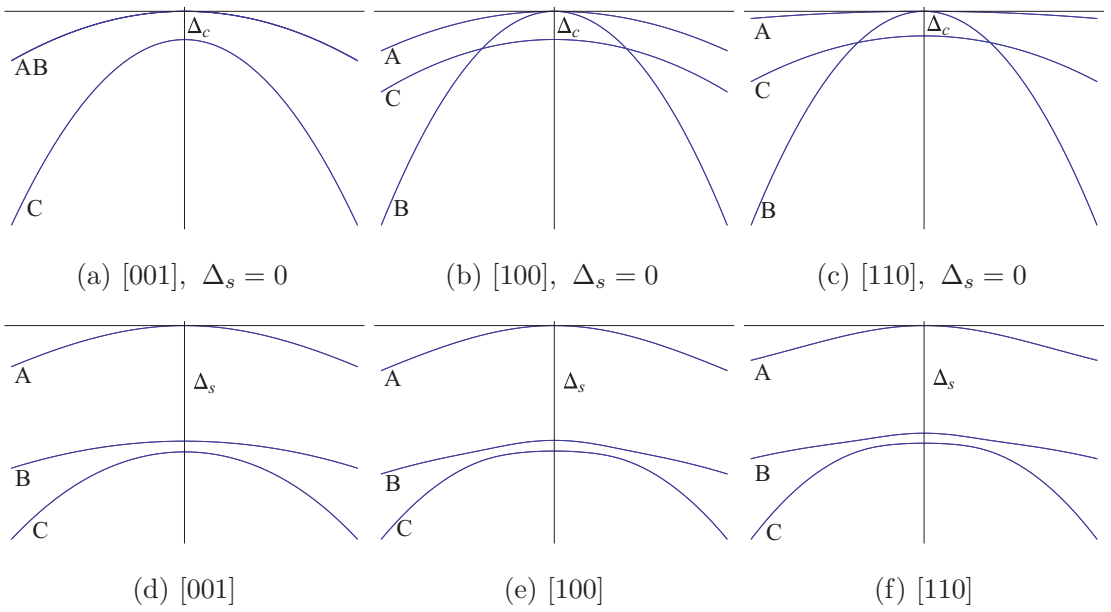

FIG. 4. (Color online) The hole dispersion in bulk $CuInS_2$ calculated along the Λ [001] Σ [100], and Δ [110] directions without and with spin-orbit splitting are shown in (a)–(c) and (d)–(f), respectively.

$m_C = 0.49m_0$ in the [100] and [110] directions. The linear invariants and the spin-orbit coupling, at energies higher than Δ_s, do not substantially contribute to the valence band structure, but they can change the optical selection rules of NCs. The effect of these invariants is considered below.

IV. ELECTRONS AND HOLES IN $CuInS_2$ NANOCRYSTALS

Using the multiband $\boldsymbol{k}\cdot\boldsymbol{p}$ effective mass Hamiltonian we can describe optical properties of small spherical $CuInS_2$ NCs. In small NCs, both holes and electrons are subjected to strong spatial confinement and the optical properties are determined by transitions between their quantum-size levels. We consider the band-edge optical transitions and hence describe only the lowest energy levels in the conduction and valence bands. In spherical NCs, the ground $1S_e$ level of the conduction band has zero angular momentum and its energy, E_{1S_e} for the infinitely high confinement barrier, is [52]

$$E_{1S_e} = \frac{\hbar^2\pi^2}{2m_0a^2}\left[\alpha + \frac{E_p}{E_g + E_{1S_e}}\right], \tag{8}$$

where a is the NC radius.

In spherical NCs the hole confined levels can be found using first order perturbation theory with the spherical Hamiltonian:

$$\hat{H}_{\text{sphere}} = \frac{1}{2m_0}[(\gamma_1 + 4\gamma)p^2 - 6\gamma(\boldsymbol{pI})^2]. \tag{9}$$

This Hamiltonian can be obtained from $\hat{H}_{\text{cubic}}$ in Eq. (2) if we neglect the hole energy spectrum warping by putting $\gamma_2 = \gamma_3 = \gamma$. For the hole confined in the spherical potential the first order corrections to the hole energy level are connected with the warping of hole energy, which is proportional to $\gamma_2 - \gamma_3$ and vanishes if one selects $\gamma = (2\gamma_2 + 3\gamma_3)/5$ [53]. For the spherical approximation in Eq. (9), we estimate $\gamma_1 = 2.63$ $\gamma = 0.73$. The Hamiltonian (9) describes the spectrum of the valence band consisting of three branches: the light-hole branch and two heavy-hole branches degenerate at $p = 0$. The effective masses of the light and heavy holes are $m_0/(\gamma_1 + 4\gamma)$ and $m_0/(\gamma_1 - 2\gamma)$, respectively. For the γ parameters obtained from our first principles calculations, the masses are $m_l = 0.18m_0$ and $m_h = 0.85m_0$.

Let us now consider the energy levels of holes in spherical $CuInS_2$ NCs with radius a, whose effective mass Hamiltonian is given by Eq. (9). The Hamiltonian (9) commutes with operator of the total momentum $\hat{\boldsymbol{F}} = \boldsymbol{I} + \hat{\boldsymbol{l}}$ $F = I + l = 0,1,2,\ldots$, whose eigenfunctions are the spherical vectors introduced in Ref. [54]:

$$\boldsymbol{Y}_{F,l,M}(\theta,\phi) = \sum_{m+\mu=M} C^{F,M}_{lm,1\mu} Y_{lm}(\theta,\phi)\boldsymbol{\chi}_\mu, \tag{10}$$

where $Y_{lm}(\theta,\phi)$ are spherical harmonics, $C^{F,M}_{lm,1\mu}$ are the Clebsch-Gordan coefficients defined in Ref. [54], and $\boldsymbol{\chi}_\mu$ are spinors representing the eigenvectors of the operator $\hat{I}_z$: $\hat{I}_z\boldsymbol{\chi}_\mu = \mu\chi_\mu$ where $\mu = \pm1,0$ and

$$\boldsymbol{\chi}_{-1} = \frac{1}{\sqrt{2}}\begin{pmatrix}1\\-i\\0\end{pmatrix}, \quad \boldsymbol{\chi}_0 = \begin{pmatrix}0\\0\\1\end{pmatrix}, \quad \boldsymbol{\chi}_1 = -\frac{1}{\sqrt{2}}\begin{pmatrix}1\\i\\0\end{pmatrix}. \tag{11}$$

In a spherical NC one can separate variables for each state with total angular momentum F. In this paper, we are interested only in the manifold of the lowest energy levels of holes with the angular momentum $F = 1$. Using techniques developed in Ref. [55] we found that wave functions of the *even* states with $F = 1$ and angular momentum projection $M = \pm1,0$, can be written

$$\Psi^+_{1,M}(\mathbf{r}) = R_0(r)Y_{00}(\theta,\phi)\boldsymbol{\chi}_M + R_2(r) \times \sum_{\mu=-1}^{1} C^{1,M}_{2,M-\mu;1,\mu} Y_{2,M-\mu}(\theta,\phi)\boldsymbol{\chi}_\mu, \tag{12}$$

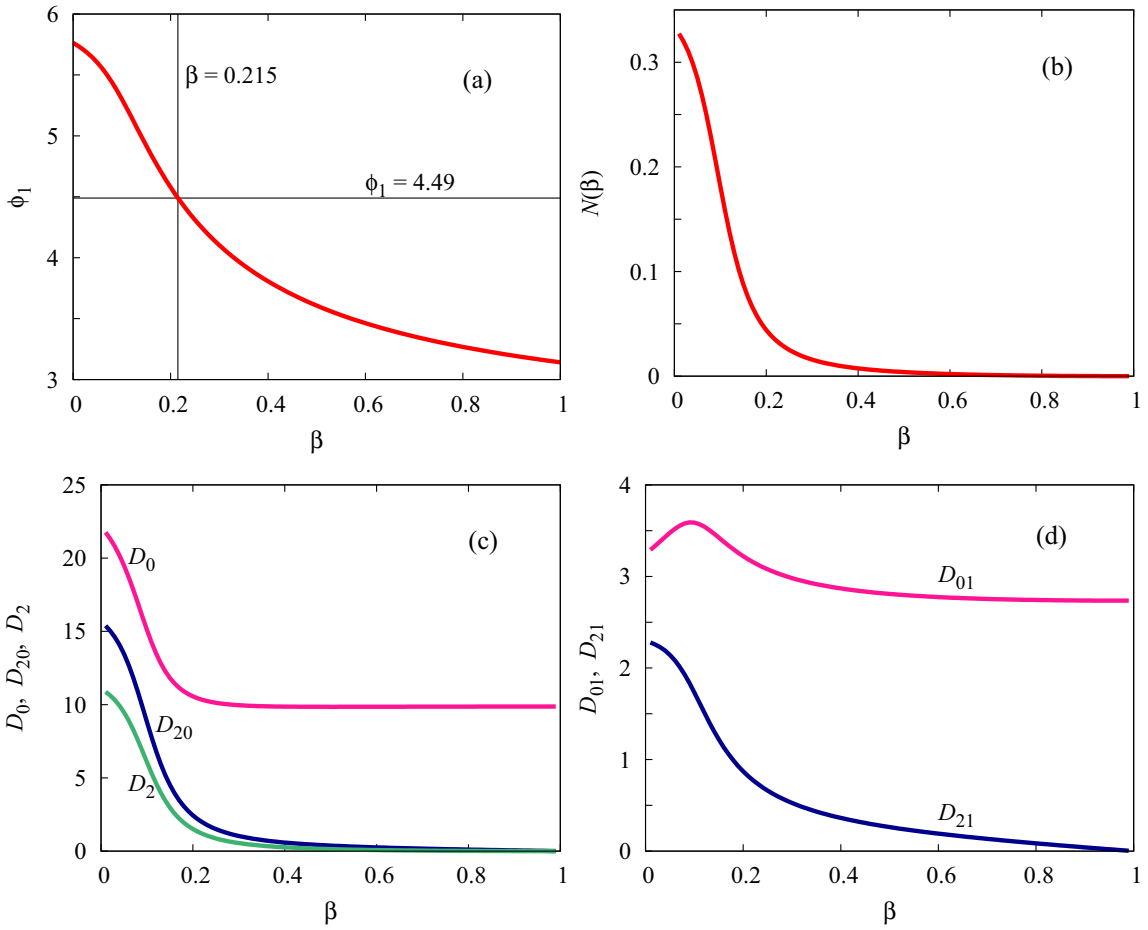

FIG. 5. (Color online) Dependence on β: (a) ϕ; (b) N; (c) D_0, D_2, and D_{20}; (d) D_{01} and D_{21}.

where

$$C^{1,M}_{2,M-\mu;1,\mu} = \begin{array}{c|ccc} {}_{\mu}{}^{M} & -1 & 0 & 1 \\ \hline -1 & \sqrt{\frac{1}{10}} & \sqrt{\frac{3}{10}} & \sqrt{\frac{3}{5}} \\ 0 & -\sqrt{\frac{3}{10}} & -\sqrt{\frac{2}{5}} & -\sqrt{\frac{3}{10}} \\ 1 & \sqrt{\frac{3}{5}} & \sqrt{\frac{3}{10}} & \sqrt{\frac{1}{10}} \end{array} . \quad (13)$$

The radial functions R_0 and R_2 satisfy the radial equations

$$\gamma_1 \hat{\Delta}_0 R_0(r) + 2\sqrt{2}\gamma \hat{A}_1 \hat{A}_2 R_2(r) = -\frac{2m_0}{\hbar^2} E R_0(r),$$
$$(\gamma_1 + 2\gamma)\hat{\Delta}_2 R_2(r) + 2\sqrt{2}\gamma \hat{A}_1^+ \hat{A}_0^+ R_0(r) = -\frac{2m_0}{\hbar^2} E R_2(r), \quad (14)$$

where E is the hole energy, $\hat{A}_l^+ = -\partial_r + l/r$, $\hat{A}_l = \partial_r + (l+1)/r$ are the raising and lowering operators [$\hat{A}_l^+ j_l(kr) = k j_{l+1}(kr)$ and $\hat{A}_l^- j_l(kr) = k j_{l-1}(kr)$], and $\hat{\Delta}_l = \partial_r^2 + (2/r)\partial_r - l(l+1)/r^2$ is the Laplacian [$\hat{\Delta}_l j_l(kr) = -k^2 j_l(kr)$].

The solution of Eq. (14) can be found as a linear superposition of spherical Bessel functions with indexes $j_0(kr)$ and $j_2(kr)$. Substituting these functions into Eq. (14), for any given energy E, we find two independent solutions $R_{0+}(r) = \sqrt{1/3}\, j_0(k_+ r)$, $R_{2+}(r) = -\sqrt{2/3}\, j_2(k_+ r)$, and $R_{0-}(r) = \sqrt{2/3}\, j_0(k_- r)$, $R_{2-}(r) = \sqrt{1/3}\, j_2(k_- r)$, where $k_\pm = \sqrt{2m_0 E/\hbar^2(\gamma_1 + \gamma \pm 3\gamma)}$. In a NC, the wave function is a linear superposition of two solutions, $b_+ R_{0+}(k_+ r) + b_- R_{0-}(k_- r)$ and $b_+ R_{2+}(k_+ r) + b_- R_{2-}(k_- r)$, which must satisfy boundary conditions at $r = a$. For an infinitely high barrier at the NC surface, the wave functions turn to zero at $r = a$, and we have

$$b_+ j_0(\sqrt{\beta}\phi) + b_- \sqrt{2} j_0(\phi) = 0,$$
$$-b_+ \sqrt{2} j_2(\sqrt{\beta}\phi) + b_- j_2(\phi) = 0, \quad (15)$$

where $\phi = k_- a$, $\phi\sqrt{\beta} = k_+ a$, and $\beta = (\gamma_1 - 2\gamma)/(\gamma_1 + 4\gamma)$ is the ratio of the light to heavy hole effective masses. The nontrivial solution of Eq. (15), $b_+ = -b_- \sqrt{2} j_0(\phi)/j_0(\sqrt{\beta}\phi)$, exists if $\phi \equiv \phi(\beta)$ is a root of the following equation:

$$j_0[\phi(\beta)\sqrt{\beta}] j_2[\phi(\beta)] + 2 j_0[\phi(\beta)] j_2[\phi(\beta)\sqrt{\beta}] = 0. \quad (16)$$

The roots $\phi_n(\beta)$ of Eq. (16) define the spectrum of energy. The lowest energy level is

$$E^+ = E_a(\gamma_1 - 2\gamma)\phi_1^2(\beta), \quad (17)$$

where $E_a = \hbar^2/2m_0 a^2$ and ϕ_1 is the first root of Eq. (16) shown in Fig. 5(a). The normalized wave functions of the *even*

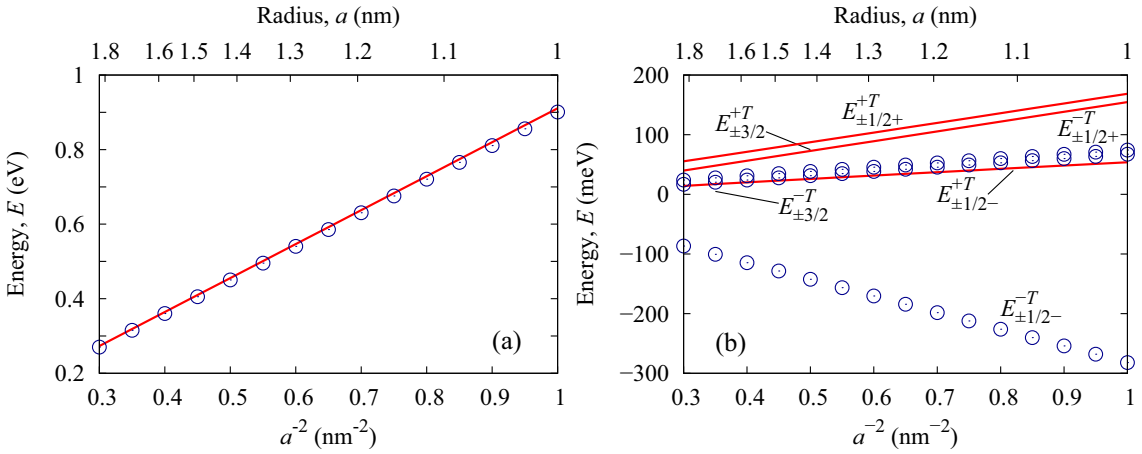

FIG. 6. (Color online) (a) Size dependence of the two lowest *odd* (blue open circles) and *even* (red lines) hole levels with $F = 1$ in spherical approximation with $\gamma_1 = 2.63$ and $\gamma = 0.73$. (b) Fine structure energy levels of holes: "even" (red lines) and "odd" (blue open circles) states split by tetragonal invariants in the Hamiltonian.

states are given by

$$R_0^+(r) = \frac{b^+}{a^{3/2}}\sqrt{2}\left[-\frac{j_0(\phi)}{j_0(\sqrt{\beta}\phi x)}j_0(\sqrt{\beta}\phi x) + j_0(\phi x)\right],$$
$$R_2^+(r) = \frac{b^+}{a^{3/2}}\left[2\frac{j_0(\phi)}{j_0(\sqrt{\beta}\phi)}j_2(\sqrt{\beta}\phi x) + j_2(\phi x)\right], \quad (18)$$

where $x = r/a$ and the constant b^+ is determined by the normalization condition: $\int_0^a r^2\,dr([R_0^+]^2 + [R_2^+]^2) = 1$.

For the *odd* states the wave function with $F = 1$ has the form

$$\Psi^-_{1,M}(\mathbf{r}) = R_1^-(r)\sum_{\mu=-1}^{1} C^{1,M}_{1,M-\mu;1,\mu}Y_{1,M-\mu}(\theta,\phi)\boldsymbol{\chi}_\mu, \quad (19)$$

where

$$C^{1;M}_{1,M-\mu;1,\mu} = \begin{array}{c|ccc} {}_{\mu}{}^{M} & -1 & 0 & 1 \\ \hline -1 & \frac{1}{\sqrt{2}} & \frac{1}{\sqrt{2}} & 0 \\ 0 & -\frac{1}{\sqrt{2}} & 0 & \frac{1}{\sqrt{2}} \\ 1 & 0 & -\frac{1}{\sqrt{2}} & -\frac{1}{\sqrt{2}} \end{array}. \quad (20)$$

The radial function $R_1^-(r)$ is a solution of the following equation:

$$\frac{\hbar^2}{2m_0}(\gamma_1 - 2\gamma)\hat{\Delta}_1 R_1^-(r) = -E R_1^-(r). \quad (21)$$

The solutions of Eq. (21) are given by $R_1^-(r) = bj_1(kr)$, where $k = \sqrt{2m_0E/\hbar^2(\gamma_1 - 2\gamma)}$ and hence $R_1^-(r)$ belong to the heavy hole states which are three fold degenerate with respect to $M = \pm 1,0$. In a spherical confinement with the infinite barrier, the radial function is zero at $r = a$. The zeros $k_n a$ of the spherical Bessel function $j_1(ka)$ correspond to the energy levels of odd states in a NC. The normalized wave functions of the lowest odd energy state is given by

$$R_1^-(r) = \frac{b^-}{a^{3/2}}j_1(\xi_1 r/a), \quad (22)$$

where b^- is determined by the normalization condition: $\int_0^a r^2\,dr[R_1^-]^2 = 1$ and $\xi_1 = k_1 a \approx 4.49$ with the corresponding energy level given by

$$E^- = E_a(\gamma_1 - 2\gamma)\xi_1^2. \quad (23)$$

Comparing ξ_1 with $\phi_1(\beta)$ in Fig. 5(a) we conclude that the *odd* state is the ground hole level in the case when $\beta < 0.215$. Our calculations shows that in $CuInS_2$ NCs this is the case since $\beta = 0.21$. This β is very close to the critical value of 0.215 and in the cubic approximation in $CuInS_2$ the *even* and *odd* states become accidentally degenerate [see Fig. 6(a).

The *odd* states are optically passive because in the spherical approximation they are composed of only p symmetry wave functions, so that optical transitions from to the ground electron level with the s symmetry are forbidden. At the same time, the *even* levels of holes with $F = 1$ are optically active because their wave functions have the s symmetry contributions, resulting in nonzero transition matrix elements. In the spherical and cubic approximations, both optically active and optically passive states are present at the absorption edge.

The tetragonal invariants in the Hamiltonian, V_{2d}, lift the threefold degeneracy of energy levels with $F = 1$ in each manifold of the *odd* and *even* states. As we show below, the tetragonal invariants substantially split the *odd* and *even* states with the *odd* levels becoming the optically passive ground state of holes. The optically passive ground state, however, is partially activated by the linear terms V'_{2d} and V''_{2d}, which mix the *even* and *odd* states.

V. FINE STRUCTURE OF THE HOLE ENERGY LEVELS

Here we consider the fine structure splitting of the lowest *even* and *odd* states, which is associated with a difference of the hole Hamiltonian $\hat{H}_{2d}$ in Eq. (4) and the spherical Hamiltonian $\hat{H}_{\text{sphere}}$ in Eq. (9). To first order, the splittings are due only to the effect of the $\hat{V}_{2\text{d}}$ invariants since the cubic corrections can be neglected, as explained above. Using Eqs. (12), (19), and (5) we find the fine structure of the *even* and *odd* energy states as a perturbation associated with the deviation from cubic symmetry and spin-orbit coupling.

Let us first consider the effect of $\Delta_c I_z^2$ term on these two levels. Both states are split into two sublevels with angular

TABLE II. Parameters for energy shifts.

Invariant	C	M	x	x_0	x_2	x_{20}
		±1	3/5	2/3	11/15	$2\sqrt{2}/15$
H_1	$\gamma_{1\perp}+4\gamma_{2\perp}$	0	4/5	2/3	8/15	$-4\sqrt{2}/15$
		±1	18/5	2	83/35	$-4\sqrt{2}/5$
H_2	$-\gamma_{2\perp}$	0	3	4	58/35	$-8\sqrt{2}/5$
		±1	0	0	1	$7/\sqrt{2}$
H_3	$\gamma_{3\perp}$	0	$-6/5$	0	18/35	0
		±1	3	2	107/35	$8\sqrt{2}/5$
H_4	$-\gamma_{4\perp}$	0	6/5	4	94/35	$-8\sqrt{2}/5$

momentum projections $M=\pm1$ and $M=0$. For the *odd* state, we have

$$E^{-}_{\pm1}=0.5\Delta_c,\quad E^{-}_{0}=\Delta_c. \tag{24}$$

For the *even* states, the energy shifts are reversed:

$$E^{+}_{\pm1}=\Delta_c[1-0.3N(\beta)],\quad E^{+}_{0}=0.6\Delta_c N(\beta), \tag{25}$$

where the function $N(\beta)=\int_0^a[R_2^+(r)]^2r^2\,dr$ is shown in Fig. 5(b) and $N(0.21)=0.04$ in $CuInS_2$ NCs.

All other terms in V_{2d} are quadratic in the momentum projections p_x, p_y, and p_z. According to Eq. (5), four quadratic invariants are $H_1=(\gamma_{1\perp}+4\gamma_{2\perp})(p_x^2+p_y^2)/(2m_0)$, $H_2=-6\gamma_{2\perp}(p_x^2I_x^2+p_y^2I_y^2)/(2m_0)$, $H_3=-12\gamma_{3\perp}\{p_x,p_y\}\{I_x,I_y\}/(2m_0)$, and $H_4=-6\gamma_{4\perp}(p_x^2I_y^2+p_y^2I_x^2)/(2m_0)$. For angular momentum projection $M=0,\pm1$, the corresponding energy shifts can be written as

$$E^{-}_{M}=Cx(M)\xi_1^2E_a \tag{26}$$

for the *odd* states and

$$E^{+}_{M}=C[x_2(M)D_2(\beta)+x_0(M)D_0(\beta)+x_{20}(M)D_{20}(\beta)]E_a \tag{27}$$

for the *even* states, where $D_2(\beta)=-a^2\int_0^a R_2^+\Delta_2R_2^+r^2\,dr$, $D_0(\beta)=-a^2\int_0^a R_0^+\Delta_0R_0^+r^2\,dr$ and $D_{20}(\beta)=a^2\int_0^a R_2^+A_1^+A_0^+R_0^+r^2\,dr$, and the coefficients C, x, x_2, x_0, and x_{20} are shown in Table II for all four invariants. The functions $D_0(\beta)$, $D_2(\beta)$, and $D_{20}(\beta)$ are shown in Fig. 5(c) and in $CuInS_2$ NCs where $\beta=0.21$, $D_2=1.34$, $D_0=10.4$, and $D_{20}=2.19$.

The total splitting of *odd* and *even* states can be found by taking a sum of all energies obtained in Eqs. (24)–(27). For the $CuInS_2$ Luttinger parameters and $\beta=0.21$, the result can be written as

$$\begin{aligned}
E_0^{+T}&=0.02\Delta_c+0.06E_a(\gamma_1-2\gamma)\phi_1^2,\\
E_{\pm1}^{+T}&=0.99\Delta_c+0.18E_a(\gamma_1-2\gamma)\phi_1^2,\\
E_0^{-T}&=\Delta_c-0.31E_a(\gamma_1-2\gamma)\xi_1^2,\\
E_{\pm1}^{-T}&=0.5\Delta_c+0.08E_a(\gamma_1-2\gamma)\xi_1^2.
\end{aligned} \tag{28}$$

The splitting between the lowest *odd* and *even* states is $E_0^{+T}-E_0^{-T}\approx-0.98\Delta_c+0.37E_a(\gamma_1-2\gamma)\xi_1^2$. This splitting, which lifts the accidental degeneracy of *odd* and *even* states, substantially increases with decrease of the NC size.

Up to this point we have neglected the spin-orbit coupling $\hat{V}_{so}$. Without it, all levels are doubly degenerate in spin projection. With spin-orbit coupling included, each of the *odd* and *even* manifolds is split in three Kramer's doublets, one with the momentum projections $\pm3/2$ and two with the momentum projections $\pm1/2$. The corresponding splittings are given by

$$\begin{aligned}
E^{\pm T}_{\pm3/2}&=\tfrac{1}{3}\Delta_s^{\pm}+E^{\pm T}_{\pm1},\\
E^{\pm T}_{\pm1/2+}&=\tfrac{1}{6}\big(3E^{\pm T}_{\pm1}+3E^{\pm T}_{0}-\Delta_s^{\pm}\big)+\tfrac{1}{6}\sqrt{9\big(\Delta_s^{\pm}\big)^2+6\Delta_s^{\pm}\big(E^{\pm T}_{0}-E^{\pm T}_{\pm1}\big)+9\big(E^{\pm T}_{0}-E^{\pm T}_{\pm1}\big)^2},\\
E^{\pm T}_{\pm1/2-}&=\tfrac{1}{6}\big(3E^{\pm T}_{\pm1}+3E^{\pm T}_{0}-\Delta_s^{\pm}\big)-\tfrac{1}{6}\sqrt{9\big(\Delta_s^{\pm}\big)^2+6\Delta_s^{\pm}\big(E^{\pm T}_{0}-E^{\pm T}_{\pm1}\big)+9\big(E^{\pm T}_{0}-E^{\pm T}_{\pm1}\big)^2},
\end{aligned} \tag{29}$$

where $\Delta_s^-=\Delta_s/2$ and $\Delta_s^+=\Delta_s[1-3N(\beta)/2]$. The size dependence of the energy levels fine structure is shown in Fig. 6(b). One can see that the splitting of the lowest optically passive, $E^{-T}_{\pm1/2-}$, and the lowest optically active, $E^{+T}_{\pm1/2-}$, states increases with decrease of NC size, and it is significantly larger than room temperature. This should result in a large Stock's shift and a long radiative decay time of the band-edge PL.

VI. ACTIVATION OF THE OPTICALLY PASSIVE GROUND HOLE STATE IN NCS

As shown above, the *odd* levels are the optically passive ground states. For PL from the ground state to be possible, the ground state needs to be admixed with an optically active state. The *odd* and *even* states, however, remain decoupled under both the tetragonal, V_{2d}, and spin-orbit, $\hat{V}_{so}$, interactions. We will now show that the linear invariants $\hat{V}'_{2d}$ and $\hat{V}''_{2d}$ in Eq. (6) result in a mixture of the *odd* states with the optically active *even* states leading to a radiative recombination of the ground exciton state.

The nonzero matrix components of the $\hat{V}'_{2d}$ invariant are

$$\begin{aligned}
\langle\Psi^+_{1,\mp1}|\hat{V}'_{2d}|\Psi^-_{1,\pm1}\rangle&=-\frac{i}{\sqrt{6}}\left[D_{01}(\beta)+\frac{2\sqrt{2}}{5}D_{21}(\beta)\right]\frac{\hbar u_I}{a},\\
\langle\Psi^+_{1,\pm1}|\hat{V}'_{2d}|\Psi^-_{1,\pm1}\rangle&=\frac{1}{\sqrt{6}}[D_{01}(\beta)+\sqrt{2}D_{21}(\beta)]\frac{\hbar\bar{u}_I}{a},
\end{aligned} \tag{30}$$

where $D_{01}(\beta)=a\int_0^a R_0^+A_1^-R_1^-r^2\,dr$ and $D_{21}(\beta)=a\int_0^a R_2^+A_1^+R_1^-r^2\,dr$ are shown in Fig. 5(d) and $D_{01}(0.21)=3.19$, $D_{21}(0.21)=0.82$ for $\beta=0.21$ in $CuInS_2$. The $\hat{V}'_{2d}$ interaction is independent of the spin of hole and the matrix components in Eq.(30) are diagonal in the hole spin projections $s_z=\pm1/2$. The $\hat{V}''_{2d}$ invariant does not conserve the spin projections $\pm1/2$,

and its matrix elements are

$$\begin{aligned}
&\langle \Psi^{+}_{1,0}(\mp 1/2)|\hat{V}''_{2d}|\Psi^{-}_{1,\pm 1}(\pm 1/2)\rangle \\
&\quad = \langle \Psi^{+}_{1,\mp 1}(\mp 1/2)|\hat{V}''_{2d}|\Psi^{-}_{1,0}(\pm 1/2)\rangle \\
&\quad = -\frac{i}{2\sqrt{3}}[D_{01}(\beta)-\sqrt{2}D_{21}(\beta)]\frac{\hbar u_\sigma}{a}, \\
&\pm\langle \Psi^{+}_{1,0}(\mp 1/2)|\hat{V}''_{2d}|\Psi^{-}_{1,\mp 1}(\pm 1/2)\rangle \\
&\quad = \pm\langle \Psi^{+}_{1,\pm 1}(\mp 1/2)|\hat{V}''_{2d}|\Psi^{-}_{1,0}(\pm 1/2)\rangle \\
&\quad = -\frac{1}{2\sqrt{3}}[D_{01}(\beta)-\sqrt{2}D_{21}(\beta)]\frac{\hbar \bar{u}_\sigma}{a}.
\end{aligned} \tag{31}$$

All these matrix elements are inversely proportional to the NC radius, a. The admixture of the lowest *odd* and *even* states is defined as the matrix element divided by the energy difference between these states, which varies as $\sim a^{-2}$ [see Fig. 6(b). As a result the admixture is proportional to a, and therefore the radiative decay rate increases with radius as a^2.

VII. DISCUSSION

Our calculations of the band-edge level structure and optical properties show that PL should have a large Stock shift in $CuInS_2$ NCs. The band-edge absorption line in these NCs is connected with transition between the $1S_e$ electron level and the *even* hole level with the total momentum $F = 1$, while PL is connected with the *odd* hole level with total momentum $F = 1$. In the smallest NCs, the energy difference between these levels can be as large as 300 meV. The lowest *odd* hole level is slightly activated optically by its admixture to the optically active *even* hole level. This effect should result in the long infrared tail of NC band-edge absorption. The tail becomes weaker in small NCs.

The symmetry of the lowest *odd* hole level suggests that the two-photon absorption band edge in these NCs is smaller than the single-photon absorption band edge. These properties are very unusual for semiconductor NCs.

The calculations of the electron and hole levels take into account the conduction band nonparabolicity and the complex six-band structure of the valence band. The effective band parameters are extracted from the results of our first principle calculations are as following. For the conduction band they are the contribution of the remote bands $\alpha = 0.48$, Kane energy parameter $E_p = 7.95$ eV, and the effective mass $m_e = 0.16m_0$. For the valence band they are Luttinger parameters $\gamma_1 = 2.63$, $\gamma_{1\perp} - 0.03$, $\gamma_2 = 0.63$, $\gamma_{2\perp} = 0.12$ $\gamma_3 = 0.8$, $\gamma_{3\perp} = 0.3$, $\gamma_{4\perp} = -0.06$, and the crystal field splitting $\Delta_c = -2.7$ meV. Our bulk results for the electron and hole masses and crystal-field splitting are in agreement with experiments [29,30]. According to our calculation, the hole mass is heavy in the [110] direction, in agreement with experimental measurements [29].

To summarize: We have conducted first principle calculations of the energy band structure of $CuInS_2$. Using the result of these calculations we obtained the effective band parameters which describe the conduction and valence band-edge energy spectra within the multiband effective mass approximation. The latter allow us to calculate the electron and hole energy levels and optical selection rules for spherical $CuInS_2$ NCs.

ACKNOWLEDGMENTS

The authors thank M. V. Yakushev for providing the latest information on the optical properties of bulk chalcopyrite compounds. A.S. acknowledges the support of the Center for Advanced Solar Photophysics (CASP), an Energy Frontier Research Center (EFRC) funded by BES, OS, U.S. DOE. M.J.M. and Al.L.E. acknowledge the financial support of the Office of Naval Research (ONR) through the Naval Research Laboratory Basic Research Program.

[1] C. Wadi, P. Alivisatos, and D. M. Kammen, Envir. Sci. Technol. **43**, 2072 (2009)
[2] M. Ch. Lux-Steiner, A. Ennaoui, Ch.-H. Fischer, A. Jäger-Waldau, J. Klaer, R. Klenk, R. Könenkamp, Th. Matthes, R. Scheer, S. Siebentritt, and A. Weidinger, Thin Solid Films **361-362**, 533 (2000).
[3] P. Jackson, D. Hariskos, E. Lotter, S. Paetel, R. Wuerz, R. Menner, W. Wischmann, and M. Powalla, Prog. Photovolt: Res. Appl. **19**, 894 (2011).
[4] J. l. Shay, S. Wagner, and H. M. Kasper, Appl. Phys. Lett. **27**, 89 (1975).
[5] A. Chirila, S. Buecheler, F. Pianezzi, P. Bloesch, C. Gretener, A. R. Uhl, C. Fella, L. Kranz, J. Perrenoud, S. Seyrling, R. Verma, S. Nishiwaki, Y. E. Romanyuk, G. Bilger, and A. N. Tiwari, Nature Mater. **10**, 857 (2011).
[6] J. M. Luther, M. Law, Q. Song, C. L. Perkins, M. C. Beard, and A. J. Nozik, ACS Nano **2**, 271 (2008).
[7] P. Nagpal and V. I. Klimov, Nature Comm. **2**, 486 (2008).
[8] H. McDaniel, A. Y. Koposov, S. Draguta, N. S. Makarov, J. M. Pietryga, and V. I. Klimov, J. Phys. Chem. C **118**, 16987 (2014).
[9] J. M. Luther, J. Gao, M. T. Lloyd, O. E. Semonin, M. C. Beard, and A. J. Nozik, Adv. Mater. **22**, 3704 (2010).
[10] J. Gao, C. L. Perkins, J. M. Luther, M. C. Hanna, H.-Y. Chen, O. E. Semonin, A. J. Nozik, R. J. Ellingson, and M. C. Beard, Nano Lett. **11**, 3263 (2011).
[11] C.-H. M. Chuang, P. R. Brown, V. Bulovic, and M. G. Bawendi, Nature Mater. **13**, 796 (2014).
[12] J. Zhang, J. Gao, C. P. Church, E. M. Miller, J. M. Luther, V. I. Klimov, and M. C. Beard, Nano Lett. **14**, 6010 (2014).
[13] I. J. Kramer, J. C. Minor, G. Moreno-Bautista, L. Rollny, P. Kanjanaboos, D. Kopilovic, S. M. Thon, G. H. Carey, K. W. Chou, D. Zhitomirsky, A. Amassian, and E. H. Sargent, Adv. Mater. **27**, 116 (2015).
[14] P. M. Allen and M. G. Bawendi, J. Am. Chem. Soc. **130**, 9240 (2008).

[15] L. Li, A. Pandey, D. J. Werder, B. P. Khanal, J. M. Pietryga, and V. I. Klimov, J. Am. Chem. Soc. **133**, 1176 (2011).
[16] H. Zhong, Z. Bai, and B. Zou, J. Phys. Chem. Lett. **3**, 3167 (2012).
[17] O. Yarema, D. Bozyigit, I. Rousseau, L. Nowack, M. Yarema, W. Heiss, and V. Wood, Chem. Mater. **25**, 3753 (2013).
[18] Q. Guo, S. J. Kim, M. Kar, W. N. Shafarman, R. W. Birkmire, E. A. Stach, R. Agrawal, and H. W. Hillhouse, Nano Lett. **8**, 2982 (2008).
[19] M. G. Panthani, V. Akhavan, B. Goodfellow, J. P. Schmidtke, L. Dunn, A. Dodabalapur, P. F. Barbara, and B. A. Korgel, J. Am. Chem. Soc. **130**, 16770 (2008).
[20] D. Aldakov, A. Lefrancois, and P. Reiss, J. Mater. Chem. C **1**, 3756 (2013).
[21] Y. Shirasaki, G. J. Supran, M. G. Bawendi, and V. Bulovic, Nature Photon. **7**, 13 (2013).
[22] H. McDaniel, N. Fuke, J. M. Pietryga, and V. I. Klimov, J. Phys. Chem. Lett. **4**, 355 (2013).
[23] H. McDaniel, N. Fuke, N. S. Makarov, J. M. Pietryga, and V. I. Klimov, Nature Comm. **4**, 2887 (2013).
[24] B. Tell, J. L. Shay, and H. M. Kasper, Phys. Rev. B **4**, 2463 (1971).
[25] J. J. M. Binsma, L. J. Ciling, and J. Bloem, J. Luminescence **27**, 55 (1982).
[26] S. Shirakata and H. Miyake, J. Phys. Chem. Solids **64**, 2021 (2003).
[27] M. V. Yakushev, A. V. Mudryi, I. V. Victorov, J. Krustok, and E. Mellikov, Appl. Phys. Lett. **88**, 011922 (2006).
[28] M. V. Yakushev, R. W. Martin, A. V. Mudryi, and A. V. Ivaniukovich, Appl. Phys. Lett. **92**, 111908 (2008).
[29] M. V. Yakushev, R. W. Martin, and A. V. Mudryi, Appl. Phys. Lett. **94**, 042109 (2009).
[30] J. L. Shay, B. Tell, H. M. Kasper, and L. M. Schiavone, Phys. Rev. B **5**, 5003 (1971).
[31] B. Gil, D. Felbacq, and S. F. Chichibu, Phys. Rev. B **85**, 075205 (2012).
[32] J. E. Jaffe and A. Zunger, Phys. Rev. B **28**, 5822 (1983).
[33] J. E. Jaffe and A. Zunger, Phys. Rev. B **29**, 1882 (1984).
[34] M. V. Yakushev, F. Luckert, A. V. Rodina, C. Faugeras, A. V. Karotki, A. V. Mudryi, and R. W. Martin, Appl. Phys. Lett. **101**, 262101 (2012).
[35] M. V. Yakushev, A. V. Rodina, G. M. Shuchalin, R. P. Seisian, M. A. Abdullaev, A. Rockett, V. D. Zhivulko, A. V. Mudryi, C. Faugeras, and R. W. Martin, Appl. Phys. Lett. **105**, 142103 (2014).
[36] J. L. Shay and H. M. Kasper, Phys. Rev. Lett. **29**, 1162 (1972).
[37] G. Brandt, A. Räuber, and J. Schneider, Solid State Comm. **12**, 481 (1973).
[38] G. Kresse and J. Hafner, Phys. Rev. B **48**, 13115 (1993).
[39] G. Kresse and J. Hafner, Phys. Rev. B **49**, 14251 (1994).
[40] G. Kresse, Ph.D. thesis, Technische Universität Wien, Vienna, 1993.
[41] P. E. Blöchl, J. Kästner, and C. J. Först, in *Handbook of Materials Modeling*, edited by Sidney Yip (Springer, Dordrecht, 2005), Chap. 1, pp. 93–119.
[42] J. P. Perdew, K. Burke, and M. Ernzerhof, Phys. Rev. Lett. **77**, 3865 (1996).
[43] P. Hohenberg and W. Kohn, Phys. Rev. **136**, B864 (1964).
[44] W. Kohn and L. J. Sham, Phys. Rev. **140**, A1133 (1965).
[45] A. V. Krukau, O. A. Vydrov, A. F. Izmaylov, and G. E. Scuseria, J. Chem. Phys. **125**, 224106 (2006).
[46] M. Lax, *Symmetry Principles in Solid State and Molecular Physics* (John Wiley, New York, 1974).
[47] Al. L. Efros and M. Rosen, Annu. Rev. Mater. Sci. **30**, 475 (2000).
[48] D. C. Look and T. C. Manthuruthil, J. Phys. Chem. Solids **37**, 173 (1976).
[49] J. M. Luttinger, Phys. Rev. **102**, 1030 (1956)
[50] G. L. Bir and G. E. Pikus, *Symmetry and Strain-Induced Effects in Semiconductors* (Wiley/Halsted Press, New York, 1974).
[51] S. Limpijumnong and W. R. L. Lambrecht, Phys. Rev. B **65**, 165204 (2002).
[52] A. I. Ekimov *et al.*, J. Opt. Soc. Am. B **10**, 100 (1993)
[53] N. O. Lipari and A. Baldereschi, Phys. Rev. Lett. **25**, 1660 (1970).
[54] A. I. Akhiezer and V. B. Berestetskii, *Quantum Electrodynamics* (Interscience Publishers, New York, 1965).
[55] A. I. Ekimov, A. A. Onuschenko, M. E. Raikh, and Al. L. Efros, Sov. Phys. JETP **63**, 1054 (1986).